ACS APPLIED MATERIALS & INTERFACES
Research Article
www.acsami.org

Rechargeable Sodium-Ion Battery: High-Capacity Ammonium Vanadate Cathode with Enhanced Stability at High Rate

Ananta Sarkar,[†] Sudeep Sarkar,[†] Tanmay Sarkar,[‡] Parveen Kumar,[‡] Mridula Dixit Bharadwaj,[‡] and Sagar Mitra*,[†]

[†] Electrochemical Energy Laboratory, Department of Energy Science and Engineering, Indian Institute of Technology Bombay, Powai, Mumbai 400076, Maharashtra India

[‡] Center for Study of Science, Technology and Policy, 18, 10th Cross, Mayura Street, Papanna Layout, Nagashettyhalli, RMV II Stage, Bangalore 560094, Karnataka India

Ⓢ *Supporting Information*

ABSTRACT: Sodium-ion battery (NIB) cathode performance based on ammonium vanadate is demonstrated here as having high capacity, long cycle life and good rate capability. The simple preparation process and morphology study enable us to explore this electrode as suitable NIB cathode. Furthermore, density functional theory (DFT) calculation is envisioned for the $NH_4V_4O_{10}$ cathode, and three possible sodium arrangements in the structure are depicted for the first time. Relevant NIB-related properties such as average voltage, lattice constants, and atomic coordinates have been derived, and the estimated values are in good agreement with the current experimental values. A screening study shows ammonium vanadate electrodes prepared on carbon coat onto Al-current collector exhibits a better electrochemical performance toward sodium, with a sustained reversible capacity and outstanding rate capability. With the current cathode with nanobelt morphology, a reversible capacity of 190 mAh g^{-1} is attained at a charging rate of 200 mA g^{-1}, and a stable capacity of above 120 mAh g^{-1} is retained for an extended 50 cycles tested at 1000 mA g^{-1} without the addition of any expensive electrolyte additive.

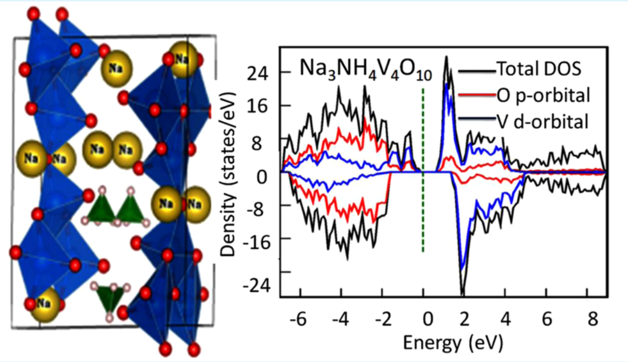

KEYWORDS: *ammonium vanadate, ab initio modeling study, cyclic stability, power performance, sodium ion battery cathode*

■ INTRODUCTION

Lithium-ion batteries (LIB) are typically material-intensive technology, and if they are to become widely deployed, the elements required by this technology will be needed in significant quantities. However, many of these elements are expensive, or traded in large quantities and as a result their availability may be constrained. The major elements like lithium, cobalt, and so on, can be considered as "critical" for a variety of reasons such as uneven distribution in earth's crust, poor concentration by natural processes, or production in a small number of countries or in locations subject to political instability.[1] Therefore, shortage of these critical elements is significantly accelerate the adoption of alternative energy storage technologies currently that could in turn limit the competitiveness of lithium-ion technologies.

Recently, there have been large efforts to identify long-term and large-scale storage technology that are both essential to our economy and able to supply adequate energy and power. One such technology is sodium-ion batteries (NIB), which are currently of significant interest mainly due to their cost advantages and the relative abundance of sodium in earth's crust compared to lithium.[1] In response to growing concerns of NIB electrode materials, a diverse range of transition metal (TM)-based oxides, phosphates, silicates, borates, pyrophosphates, fluoro-phosphates, and fluoro-sulfate materials have been explored as positive electrode materials, as similar approach adopted in LIBs.[1−8] However, low discharge capacity, cyclic stability, and lack of proper electrolyte combinations make NIB very attractive to the academic researchers to perform science.

Fundamentally, the ionic volume of Na is more than 70% larger than that of Li, and it could be more prominent in solvated state. The larger sized cations need large open framework to facilitate cations intercalation/deintercalation in the host electrode. In response to this problem, several groups have demonstrated layered transition metal oxides with orthorhombic, monoclinic crystal structure that can be used as cathode materials for a NIB. Similarly, vanadium oxide could be considered as a prominent cathode material due to its layered structure that can facilitates cation insertion and

Received: April 14, 2015
Accepted: July 20, 2015
Published: July 20, 2015

DOI: 10.1021/acsami.5b03210

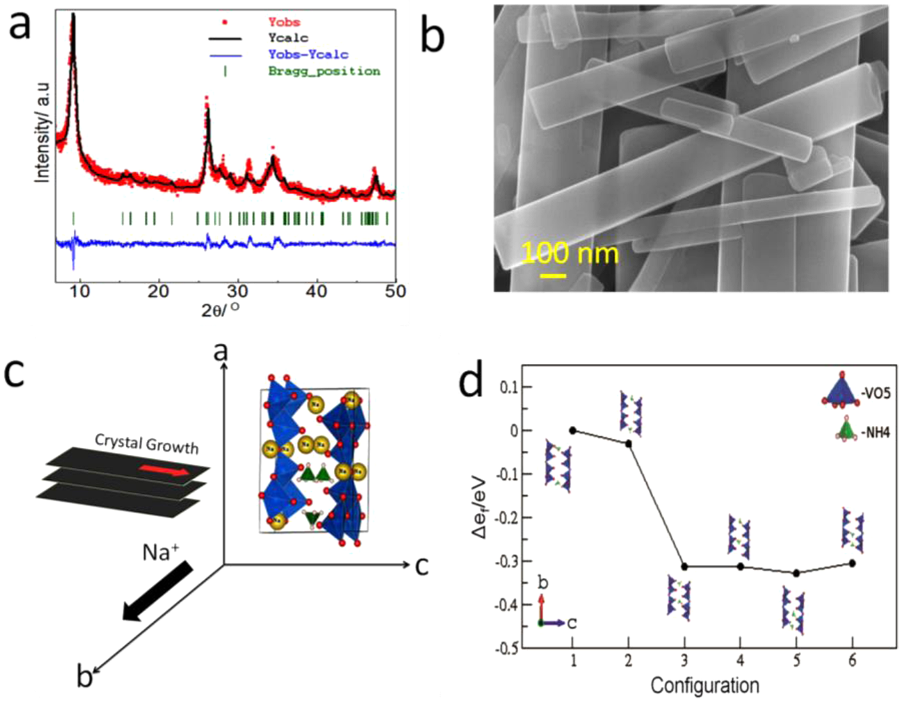

Figure 1. (a) XRD pattern of $NH_4V_4O_{10}$ sample. (b) FEG-SEM image of $NH_4V_4O_{10}$. (c) Graphical representation of $NH_4V_4O_{10}$ nanobelts growth. (d) Formation energy differences of different configurations of $NH_4V_4O_{10}$ from DFT calculations.

extraction within its framework without generating much mechanical stress.[9] In this direction, many studies have recently attempted to increase the interlayer spacing and surface area of vanadium oxide.[10,11]

Recently, we have reported lithium trivanadate ($Li_xV_3O_8$)[12,13] and $NH_4V_4O_{10}$[14] with quasi-one-dimensional morphology as LIB cathode materials where both of these electrodes can accommodate more than two lithium[12−14] or sodium-ions in their structure without much distortion. However, sodium intercalation in ammonium vanadate cathode was not successful in the past, and few reports showed gradual capacity fading at very low current rates.[15,16] In principle, after insertion and deinsertion of Na^+ in the host matrix, the reaction should keep the host structure intact. However, the large variation in sodium content within the electrodes during continuous cycling may cause a diverse range of structural changes, such as lattice expansion or contraction, order−disorder transition, two-phase reaction, phase separation, and so on.[17] Such changes arise locally at the atomic level, impose a significant influence on Na^+ reactivity, and determine the overall cyclic performance of NIBs. Therefore, it is anticipated here that any new electrode material need to be characterized on the basis of structural changes associated with sodium insertion/extraction, and simultaneously, we gain knowledge of their energy storage mechanisms. The current study is devoted to the same goal, where ammonium vanadate acts as a cathode material for NIBs, and we intended to study from synthesis and characterization to ab initio DFT calculation and to understand the underlying phenomena of sodium reaction with electrode to improve the battery performance further.

■ EXPERIMENTAL SECTION

Synthesis. Ammonium vanadium oxide ($NH_4V_4O_{10}$) with nanobelt morphology was prepared by hydrothermal synthesis process. The synthesis procedure of $NH_4V_4O_{10}$ was adopted from our previous report.[14] In this typical synthesis process, 2.0 g of vanadium pentoxide (V_2O_5, Sigma-Aldrich, 99.6%) was added into 10 mL of ammonium hydroxide solution (NH_4OH, Merck India, 30%), and immediate color change from yellow to white was observed. Later, 80 mL of 0.1 M oxalic acid (Fisher Scientific, 99.5%) was added to the solution, and the solution was stirred continuously for 20 min. Further, pH of the solution was maintained ∼3 by dropwise addition of hydrochloric acid (HCl, Merck, 37%) which leads to color change from white to red. Immediately, the solution was further transferred into 100 mL Teflon lined autoclave and heated at 190 °C for 5 h to achieve the desired morphology. The final product was washed several times with deionized (DI) water and dried at 60 ± 5 °C in a vacuum oven and finally stored in argon filled glovebox.

Material Characterizations. The electrode materials were systematically examined by X-ray diffraction (XRD) technique at room temperature using Rigaku Smartlab X-ray diffractometer with Cu Kα radiation (λ = 1.5418 Å). A field emission gun scanning electron microscope (FEG-SEM, Carl Zeiss, Ultra-55) with a resolution about 0.8 nm and field emission gun transmission electron microscope (FEG-TEM, JEM-2100F) was used to study the morphology of the material. X-ray photoelectron spectroscopy (XPS, AXIS Ultra) was used to confirm the oxidation state of vanadium.

Electrochemical Characterizations. All electrochemical experiments were done by using lab scale Swagelok type cells. The cells were assembled inside the argon-filled glovebox (Unilab Plus, MBraun, Germany) with controlled moisture and oxygen level of 1 ppm. Ammonium vanadium oxide ($NH_4V_4O_4$) was used as a working electrode, and polished sodium foil was pasted onto a stainless steel disk to act as counter and reference electrodes in a two-electrode configuration. A borosilicate glass microfiber filter (GF/D Whatman) soaked in 1 M $NaClO_4$ in ethylene carbonate (EC)/polyethylene carbonate (PC) (1:1 wt %) was used as a separator. The electrode was prepared by mixing $NH_4V_4O_{10}$ as an active material, carbon black (Super C-65, Timcal, Switzerland), and carboxy methyl cellulose sodium salt (CMC, Loba-Chemie) in a weight ratio of 7:2:1, respectively. Water was used as a solvent to obtain a homogeneous and thick slurry, which was cast onto aluminum foil and dried at 60 ± 5 °C in a vacuum oven. The galvanostatic charge/discharge tests were carried out in an Arbin batter testing instrument (BT-2000 model,

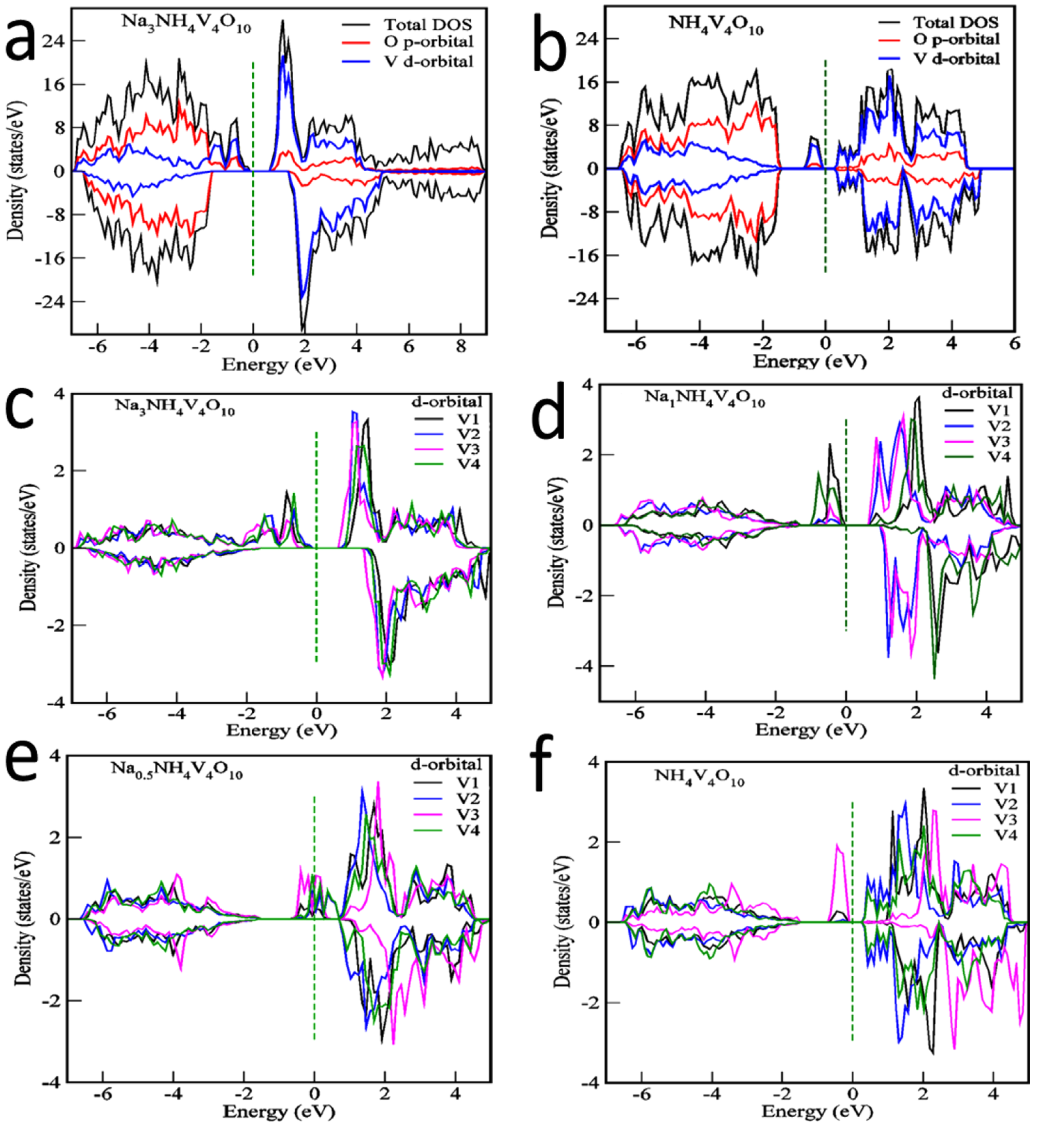

Figure 2. Density of states for (a) $Na_3NH_4V_4O_{10}$ and (b) $NH_4V_4O_{10}$. Partial density of states for d states of different types of V in (c) $Na_3NH_4V_4O_{10}$, (d) $Na_1NH_4V_4O_{10}$, (e) $Na_{0.5}NH_4V_4O_{10}$, and (f) $NH_4V_4O_{10}$ (dashed vertical line denotes Fermi level).

Arbin Instruments, College Station, TX) at various current and voltage range. Cyclic voltammetry (CV) and impedance spectroscopy experiments were carried out in a Bio-Logic potentiostat (VMP-3 model, Bio-Logic Science Instruments, France) at constant scan rate of 0.1 mV s^{-1} at various voltage ranges at controlled temperature of 20 ± 2 °C. An electrochemical impedance spectroscopy (EIS) study was performed by applying a current of 10 mA g^{-1} during the charge/discharge process in a frequency range of 1 MHz to 0.1 Hz.

■ RESULTS AND DISCUSSION

In Na or Li battery systems, solid-state insertion is generally considered as a rate-determining step among all other process such as charge transfer reaction at the interface between electrode and electrolyte, ion transport (Na/Li-ion movement through the electrolyte), and ion (electrolyte) transport inside the electrode structure.[18] Herein, we report one-dimensional (1-D) $NH_4V_4O_{10}$ nanobelts that can offer a better Na-ion kinetics within the solid-state electrode material due to low dimensionality factor and having a larger van der Waals gap between two vanadate layers. Therefore, an attempt to synthesize 1-D ammonium vanadate ($NH_4V_4O_{10}$) with minimum dimension along [0*k*0] can lead to faster Li/Na-ions kinetics, as the diffusion pathway of Li/Na-ion along the *b* axis is similar to that of the V_6O_{13} structure.[19] Further, the diffusion pathway of Li/Na-ion is along the *b* axis in $NH_4V_4O_{10}$, which is similar to V_6O_{13} structure;[19] so, an attempt to synthesize 1-D $NH_4V_4O_{10}$ with minimum dimension along [0*k*0] can lead to faster Li/Na-ions kinetics.

Here, a single-step synthesis process was adopted to prepare $NH_4V_4O_{10}$ nanobelts. In the present report, the optimum conditions for preparation of $NH_4V_4O_{10}$ nanobelts were used as previously reported literature from our group.[14] Figure 1a, shows the XRD pattern of $NH_4V_4O_{10}$ as-synthesized powder. The XRD pattern of $NH_4V_4O_{10}$ resembles monoclinic structure with high intensity peak (00*l*), which symbolizes the preferential growth of $NH_4V_4O_{10}$ material along *z* direction (or, *c* axis). The lattice parameters of $NH_4V_4O_{10}$ was evaluated by FullProf Suite.[20] The lattice parameters are a = 11.71 Å, b = 3.76 Å, c = 9.85 Å, α = 90, β = 101, and γ = 90, with space group *C*12/*m*1, which matches with standard JCPDS data (file no. 31-0075) a = 11.71 Å, b = 3.66 Å, c = 9.72 Å, α = 90, β = 101, and γ = 90. It is interesting to note from our previous study[14] that at pH ~3, $NH_4V_4O_{10}$ nanobelts not only showed

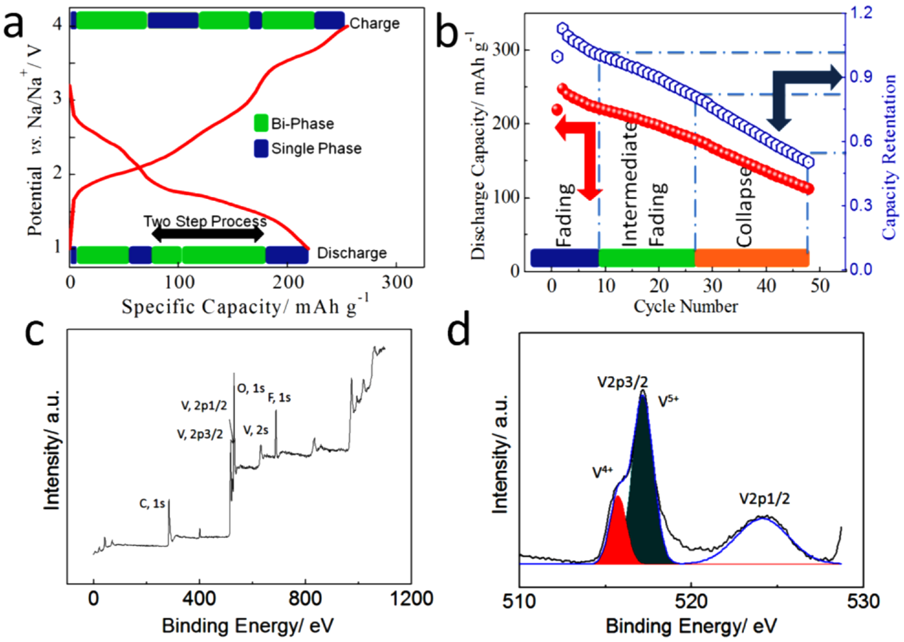

Figure 3. (a) The first charge/discharge profile at constant current (200 mA g^{-1}) charge−discharge test. (b) Discharge capacity and capacity retention vs cycle number of $NH_4V_4O_{10}$ cathode, (c) XPS survey scan of $NH_4V_4O_{10}$ cathode. (d) XPS spectrum of vanadium for $NH_4V_4O_{10}$ cathode.

perfect crystal growth but also deliver an excellent electrochemical performance against Li/Li^+.[14] The $NH_4V_4O_{10}$ nanobelts grow a few micrometers in length with a few nanometers width and thickness, as shown in Figure 1b. The material and electrochemical performance of $NH_4V_4O_{10}$ nanobelts prepared at pH ∼ 3 (temperature ∼190 °C, time ∼5 h) were discussed in detailed in present report. From Figure 1c, it can be noticed that the growth of $NH_4V_4O_{10}$ nanobelts form one-dimensional array that developed parallel to the *c* axis (*z* axis), where the *b* axis is the active site for Na^+ ion intercalation/deintercalation. Practically, all the NH_4^+ sites are in the gallery space of the $NH_4V_4O_{10}$ structure, further suggesting that facile Na^+ ion intercalation/deintercalation could happen in the same site along perpendicular *c* axis (or *z* direction). Thus, the 1-D array of ammonium vanadate allows a shorter path through the core of the particles to the surface,[18] which leads to excellent electrochemical performance in the sodium cathode.

Theoretical Calculation. To gain insight into the structural and electronic changes during insertion of Na^+ ions in $NH_4V_4O_{10}$, we also performed ab initio calculations. In the initial structure, the NH_4^+ ions lie in a gallery space of VO layers and probably interact with these VO layers via N−H...O hydrogen bonds. There are four sites available for the NH_4^+ in a gallery space with only two nonequivalent pairs of sites due to the partial occupancy of N sites. As shown in Figure 1d, we have calculated the formation energy of the different configurations of $NH_4V_4O_{10}$. Each configurations of $NH_4V_4O_{10}$ with the same site for the N have different orientational arrangement of the NH_4 molecules. For example, the location of NH_4^+ is the same in configurations 1 and 2, but the orientation of the NH_4 molecules at these sites is different. Further, our analysis of the selected lowest energy configuration suggests that the gallery space and site within VO layers are the most favorable ion insertion sites (Figure 1c).

In Figure 2, we show the density of states (DOS), partial density of states (PDOS), and V−d states at different concentration of Na from DFT calculations. As shown in Figure 2a, the valence band near the Fermi level is formed by the hybridization of O 2p states and V 3d states. During Na deintercalation, V 3d states shifted to the right with respect to the Fermi level. This suggests the major role of V^{4+}/V^{5+} redox couple during the extraction of Na^+ ion from $Na_3NH_4V_4O_{10}$ (Figure 2b). In Figure 2c−f, we compare the PDOS of four types of V at different concentrations of Na. The difference in the electronic structure of the four V types is quite apparent from Figure 2. From DFT calculations, there were three possible sodium arrangements in the structure with monoclinic system. The crystal structures of $NH_4V_4O_{10}$, $Na_1NH_4V_4O_{10}$, $Na_{0.5}NH_4V_4O_{10}$, and $Na_3NH_4V_4O_{10}$ are shown in Figure S1.

On partial Na intercalation in $NH_4V_4O_{10}$, the 3d states of V3 type shifts to the right with respect to Fermi level which on further Na intercalation shifts back to left, suggesting oxidation of V^{4+} to V^{5+} on insertion of 0.5 mole fraction of Na and reduction of V^{5+} to V^{4+} at the higher concentration of Na intercalation. Also, the band gap reduces to zero on the insertion of 0.5 mole fraction of Na in $NH_4V_4O_{10}$, which suggests transformation from semiconductor to metallic character. At higher concentrations of Na, the lower band gap (< 1 eV) suggests the semiconductor behavior of the material, which can facilitate material to perform at high charge−discharge rate. The PDOS calculation indicates the V^{4+}/V^{5+} ratio to be 2:6 in the two formula units of $NH_4V_4O_{10}$ structure. Further, the magnetic moment of V varies between 0.0 and 1.1 μB, which suggests the variation of the oxidation state of V between 4+ and 5+ during sodium deintercalation (Table S1). The presence of mixture of V^{4+} and V^{5+} influences the voltage profile and explains the existence of voltage steps at different level of Na intercalation in $Na_xNH_4V_4O_{10}$.

The presence of mixture of oxidation states may also influence the local coordination environment of the V atom, which in turn can alter the geometrical structure. The calculated lattice parameters and lattice volume for $Na_xNH_4V_4O_{10}$ (where $x = 0.0, 0.5, 1$, and 3) are listed in Table S2. On the insertion of Na ion into the gallery space (when $x < 1$ in $Na_xNH_4V_4O_{10}$; the formation energies of $NH_4V_4O_{10}$ structure with Na in gallery space is shown in Figure S2), the lattice parameters *a* and *b*

DOI: 10.1021/acsami.5b03210
ACS Appl. Mater. Interfaces 2015, 7, 17044−17053

increase by 3 and 0.8%, respectively, whereas lattice parameter *c* decreases by 7%, which results in the decrease in lattice volume by 4%. On further insertion of Na (when $x > 1$ in $Na_xNH_4V_4O_{10}$) within the VO layer, the lattice parameters *a*, *b*, and *c* increase by 4, 5, and 9%, respectively, resulting in the overall increase in lattice volume by 17%. This suggests that the insertion or extraction of Na within the VO layers leads to distortion in the structural framework of $NH_4V_4O_{10}$.

Electrochemical Performance. The utility of $NH_4V_4O_{10}$ nanobelts as cathode material has been reported for LIBs; however, electrochemical stability in this cathode material was an issue in most of the reports. The electrochemical stability was resolved by replacing commercial binder PVdF to interactive binder like CMC, previously reported by our group.[14] We believe here that the $NH_4V_4O_{10}$ nanobelts can be one of the suitable candidates for NIBs due to availability of large gallery space that can accommodate Na^+. Figure 3a,b shows the electrochemical performance of $NH_4V_4O_{10}$ cathode material against Na/Na^+ redox couple. Particularly, Figure 3a shows the intercalation/deintercalation of Na^+ for $NH_4V_4O_{10}$ cathode. The open circuit potential (OCP) of $NH_4V_4O_{10}$ cathode material against Na/Na^+ can be derived from Nernst equation, which is equal to the difference of the Na chemical potentials between two electrodes and is given by eq 1:[21,22]

$$V = -\left(\frac{\mu_{Na}^{NH_4V_4O_{10}} - \mu_{Na}}{e}\right) \tag{1}$$

where *e* is the electron charge and $\mu_{Na}^{NH_4V_4O_{10}}$ (eV per Na atom) is the Na chemical potential of the cathode. The chemical potential of intercalated Na is equal to the derivative of the free energy of the material with respect to Na concentration which is according to eq 2[21,22]

$$\mu_{Na} = \left(\frac{\delta g}{\delta x}\right)_{T,P,x} \tag{2}$$

where *g* is the Gibbs free energy per $Na_xNH_4V_4O_{10}$ formula unit, *x* is the fraction of available interstitial sites occupied by Na,[21,22] *T* is temperature, and *P* is pressure. The Gibbs phase rule in a closed system at equilibrium gives the relation among degree of freedom (DOF, *f*), the number of separate phases (*p*) and the independent components (*c*),

$$f = c - p + n \tag{3}$$

where *n* is the number of the intensive variables; however, temperature and pressure are intensive in electrochemical study. Thus, eq 3 becomes,

$$f = c - p + 2 \tag{4}$$

In NIB, the electrode can be considered as a binary system with sodium and the intercalated host. Further, fixing temperature and pressure, eq 4 becomes

$$f = (2 - p + 2) - 2 = 2 - p \tag{5}$$

For single phase ($p = 1$), from eq 5, $f = 1$, thus only one variable can vary. In electrochemical system, the potential of the cell varies with concentration (sodium). Moreover, for biphasic system ($p = 2$), $f = 0$; thus, potential (intensive variable) remain constant. Therefore, the plateaus and steep fall in charge/discharge profile show intercalation of Na^+ at various steps in the gallery space of $NH_4V_4O_{10}$ cathode material, which resembles biphasic and single-phase processes, respectively, according to the Gibbs phase rule.

The color strips shown in the Figure 3a show the region of single and biphase; however, for the ∼1.9−1.5 V region, the insertion of Na^+ was observed to be a two-step processes. Further, Figure 3b shows the discharge capacity of $NH_4V_4O_{10}$ (vs Na/Na^+) cathode material against cycle number. The first discharge capacity of $NH_4V_4O_{10}$ was ∼219 mAh g^{-1} at 200 mA g^{-1} current rate between 1 and 4 V (vs Na/Na^+) potential window. The ratio of V^{5+}/V^{4+} is in the order of 3:1, where complete reduction of V^{5+} to V^{4+} should theoretically deliver a capacity of ∼210.5 mAh g^{-1}. The extra capacity during the discharge process may be attributed to either a certain amount of V^{4+} reduction to V^{3+}[23] or to surface storage of Na^+ at low potential, which is similar to LIB. Though the initial capacity of $NH_4V_4O_{10}$ was high, after the 29th−30th cycle, the capacity fading was significant and leads to a poor electrochemical performance. At the 50th cycle, the $NH_4V_4O_{10}$ cathode holds only 51% of its initial capacity. Therefore, it is necessary to know the capacity fading mechanism of $NH_4V_4O_{10}$ cathode in the potential window of 1−4 V. X-ray photoelectron spectroscopy (XPS) was performed to determine the charge state of vanadium in $NH_4V_4O_{10}$ cathode material (Figure 3c). Figure 3d illustrates the spectrum of vanadium peaks of V 2p, which corresponds to V 2p3/2 and V 2p1/2 of V^{5+}. However, the peak ∼517.1 eV was deconvoluted to less intense peak (515.7 eV) which corresponds to V^{4+}, suggesting the coexistence of the V^{5+}/V^{4+} redox couple in $NH_4V_4O_{10}$. Moreover, to determine the ratio of V^{5+}/V^{4+} in $NH_4V_4O_{10}$ cathode material, the peak area was integrated which determine the ratio for V^{5+}/V^{4+} ∼3.07:1.

Morphology Change with Cycle Number. Figure 4a shows the morphology of pristine $NH_4V_4O_{10}$ before charge/discharge process. The nanobelts are grown in 1-D with sharp facets/or smooth edge, as shown in Figure 4a,b. The FEG-SEM image is shown in Figure S3, where smooth nanobelts with lengths of a few micrometers, width of 50−100 nm, and thickness of 10−20 nm were observed. To determine the

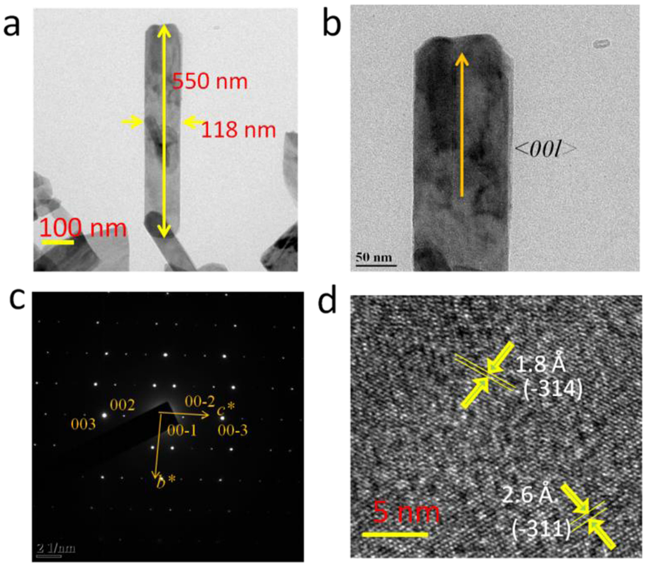

Figure 4. (a and b) FEG-TEM image of $NH_4V_4O_{10}$ material. (c) Selected area electron diffraction (SAED) of $NH_4V_4O_{10}$. (d) Lattice fringe of $NH_4V_4O_{10}$ cathode material (before charge/discharge).

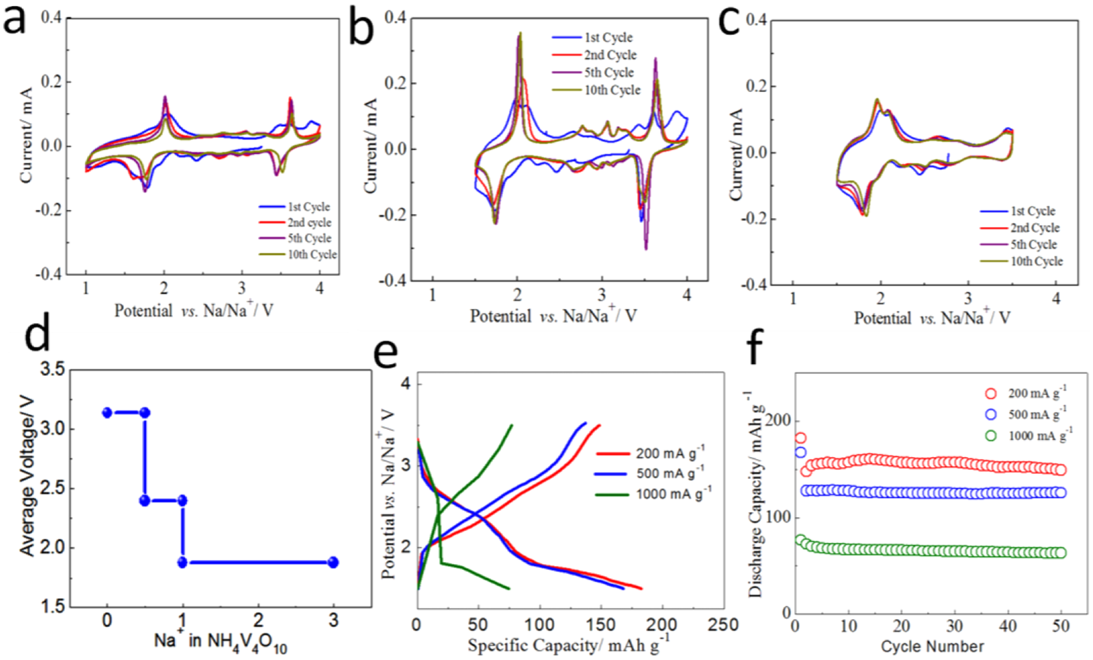

Figure 5. (a) Cyclic voltammetry of $NH_4V_4O_{10}$ cathode material at a scan rate of 0.1 mV s^{-1} in potential windows of (a) 1−4 V, (b) 1.5−4 V, and (c) 1.5−3.5 V vs Na/Na^+. (d) Calculated voltage profile of Na in $Na_xNH_4V_4O_{10}$. (e) First charge/discharge of $NH_4V_4O_{10}$ cathode material between 1.5 and 3.5 V at varying current rate. (f) Discharge capacity vs cycle number between 1.5 and 3.5 V at varying current rate.

growth of $NH_4V_4O_{10}$ nanobelts, we carried out a detailed FEG-TEM study. Figure 4b illustrates FEG-TEM image of $NH_4V_4O_{10}$ nanobelts which grows along ⟨00l⟩ direction which was confirmed by SAED pattern shown in Figure 4c. The SAED pattern of $NH_4V_4O_{10}$ was simulated with the help of Single Crystal (Crystal Maker) software, which shows the growth of the material along d_{001} direction (Figure 4c). Further, Figure 4d shows the HR-TEM image which depicts the lattice fringes of $NH_4V_4O_{10}$ material. The observed plane spacing are corresponds to $NH_4V_4O_{10}$ material with d_{-311} = 2.6 Å, and d_{-314} = 1.8 Å (JCPDS file no. 31-0075), respectively. Moreover, after continuous current charge/discharge process, the material starts degrading as observed from FEG-TEM study. The smooth edge turns of $NH_4V_4O_{10}$ material convert to rough edges with certain destruction from its initial morphology (Figure S4 shows the FEG-TEM image of $NH_4V_4O_{10}$ material after 25 cycles). With further cycling (at 32 cycles, Figure S5), the cracking was observed in the material which may be the cause of capacity fading. From the morphology study, it is well illustrated that due to destruction of $NH_4V_4O_{10}$ material, Na^+ movement along perpendicular to the *c* axis was hinder which leads to a poor electrode performance in the potential window range of 1−4 V vs Na/Na^+.

Redefining Stable Potential Window. Cyclic voltammetry (CV) study of $NH_4V_4O_{10}$ cathode material between varying potential window at a scan rate of 0.1 mV s^{-1} was performed and is shown in Figure 5a−c. CV of $NH_4V_4O_{10}$ material shows multiple cathodic/anodic peaks which resemble insertion of Na^+ ions in multiple step process where V^{5+} reduces to V^{4+}. Because of layered $NH_4V_4O_{10}$ structure, Na^+ can occupy the gallery space between vanadium−oxygen layers, the intercalation mechanism could be realized as xNa + $NH_4V_4O_{10}$ ↔ $Na_xNH_4V_4O_{10}$, which is similar to lithium intercalation reaction in $NH_4V_4O_{10}$ and V_6O_{13} cathodes.[14,24] Figure 5a shows the CV for the voltage cutoff of 1−4 V which has a prominent redox peak at 1.8 V with some minor peaks observed at 2.3, 2.5, and 3.6 V. After the second cycle, peak ∼3.6 V becomes more prominent compared to first cycle. It is noteworthy to mention here that the CV study of the region between 1 and 4 V shows an irreversible capacity loss at 3.75 V, which disappeared after the first cycle. However, there was a substantial amount of capacity fading as depicted by a decrease in the area under the curve, which is similar to the profile of discharge capacity vs cycle number (Figure 3b). Similarly, CV for the cutoff potential between 1.5 and 4 V shows (Figure 5b) a similar behavior also in the range of 1−4 V. Further, we can conclude from this section that losses that occurred during the charge/discharge process were due to an irreversible peak at ∼3.75 V and continuous fading in the 3.6 V peak region. To validate the above point, we carried out CV between 1.5 and 3.5 V at same scan rate. It can be seen from Figure 5c that all the CV profiles during the 1st, 2nd, 5th and 10th cycle overlapped each other with very minor change, which suggests the reversibility of Na^+ intercalation into the bilayer of V_2O_5 structure. Thus, the region between 1.5 and 3.5 V will deliver better cyclic stability compared to other potential window and further all other electrochemical tests were performed in this potential window.

To get an idea about the insertion process in this cathode, we performed a theoretical study. During Na^+ intercalation in $NH_4V_4O_{10}$, Na^+ first occupies the gallery space followed by the site within the VO layer. It is interesting to see how the presence of two different sites for Na intercalation can influence the voltage profile. Figure 5d shows the voltage profile of Na intercalation in $NH_4V_4O_{10}$ which exhibits plateaus at 3.14, 2.4, and 1.88 V corresponding to the insertion of 0.5, 1, and 3 mol of Na, respectively, in the host structure. The voltage plateaus at 2.4 and 1.8 V match with the experimental observations of discharge profile (Figure 5e). The large voltage gaps between the plateaus suggest the perturbation in the structural framework at each level of Na insertion.

Furthermore, cycle life and voltage profiles of NaǀElectrolyteǀ$NH_4V_4O_{10}$ cell assembly cycled between 1 and 4 V, 1.5−4 V

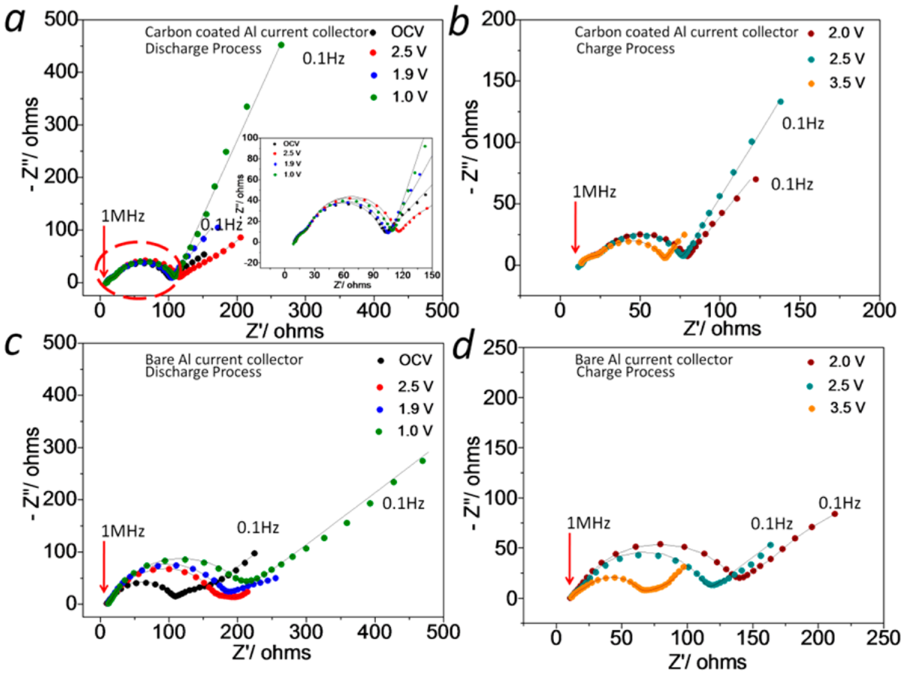

Figure 6. EIS of $NH_4V_4O_{10}$ on carbon-coated Al foil during (a) discharge process and (b) charge Process. EIS $NH_4V_4O_{10}$ on bare Al-foil during (c) discharge process and (d) charge process.

and 1.5−3.5 V at constant current was studied and is shown in Figure S6a,b. Figure S6a shows the first charge/discharge profile at constant current rate of 200 mA g^{-1} at various cutoff potentials. It is noticeable from Figure S6a that the first discharge capacity achieved by $NH_4V_4O_{10}$ was ∼246, 190, and 182 mAh g^{-1} for voltage cutoff regions of 1−4, 1.5−4, and 1.5−3.5 V, respectively. Though its theoretical capacity for three Na^+ ion intakes is ∼210.5 mAh g^{-1}, the extra capacity may be attributed to reduction of V^{4+} to V^{3+} or due to interfacial surface storage of Na^+. Figure S6b shows discharge capacity of $NH_4V_4O_{10}$ cathode material between varying potential windows for 50 cycles at constant current rate of 200 mA g^{-1}. The cutoff potential range of 1.5−3.5 V provides a greater stability compared to other potential windows, as observed in Figure S6a,b. So, it was obvious that the peaks observed at 3.75 and 3.6 V, corresponding to irreversible reactions, may be the reason behind the performance degradation of $NH_4V_4O_{10}$ cathode material. In Figure S6b, the first discharge capacity of $NH_4V_4O_{10}$ for 1.5−4 V cutoff was slightly smaller compared to the potential cutoff of 1.5−3.5 V; however, from the second cycle, the discharge capacity of 1.5−4 V cutoff remains higher compared to 1.5−3.5 V. Further, due to the irreversible peak at ∼3.75 V, the discharge capacity of $NH_4V_4O_{10}$ between 1.5 and 4 V decreases with cycling, whereas discharge capacity between 1.5 and 3.5 V cutoff remains steady.

High Rate Performance. Figure 5e shows the charge/discharge profile of $NH_4V_4O_{10}$ cathode material between 1.5 and 3.5 V potential cutoff at varying current rates. It is observed from Figure 5e that with increase in the current rate, the polarization losses increase. There was an initial loss in the first cycle; however, capacity retention was excellent throughout 50 cycles. Figure 5f shows the discharge capacity vs cycle number at current rates of 200, 500, and 1000 mA g^{-1}. First discharge capacity of $NH_4V_4O_{10}$ cathode material between 1.5 and 3.5 V were observed about ∼182, 170, and 75 mAhg^{-1} and at 200, 500, and 1000 mA g^{-1}current rate, respectively. After 50 cycles, the discharge capacities were observed to be ∼149.27, 125.95, and 63.48 mAh g^{-1} (capacity retention of 95, 98, and 85%, respectively) at the current rate of 200, 500, and 1000 mA g^{-1}, respectively. The current high rate performance of vanadium based cathode is first time in the NIB literature.

Modified Current Collector-Material Interface. The stabilization of $NH_4V_4O_{10}$ cathode material in the potential window of 1.5−3.5 V was excellent at most of the current rates; however, to improve it further, we coated the aluminum current collector with thin layer of conductive carbon. First, conductive carbon and PVdF binder was mixed in 9:1 weight ratio and dispersed in NMP solvent and with the help of acetone homogeneous slurry was made. The slurry was coated onto aluminum foil with help of a doctor blade, and the whole assembly was dried over vacuum at 60 °C and used as current collector. Further, the electrodes were prepared on a carbon-coated aluminum-foil current collector, as mentioned in the Experimental Section. The first constant current charge/discharge profile (1.5−3.5 V) shows improvement in the initial specific capacity (Figure S6c). Initial discharge capacities were observed around ∼191, 170, and 125 mAh g^{-1} at current rates of 200, 500, and 1000 mA g^{-1}, respectively. Further, compared to electrodes prepared on bare aluminum current collectors, the performance of carbon coated aluminum current collectors showed better performance that further suggests electrode-current collector interface plays a pivoting role in power performance on electrode performances. After 50 cycles, discharge capacities were observed to be ∼167 (88% retention), 135 (80% retention) and 112 mAh g^{-1} at current rates of 200, 500, and 1000 mA g^{-1}, respectively (Figure S6d).

Electrochemical Impedance Spectroscopy (EIS) Study. To investigate the improved performance of $NH_4V_4O_{10}$ cathode with carbon coated Al current collector, EIS was performed at slow current rate (10 mA g^{-1}). Figure 6 shows the impedance of $NH_4V_4O_{10}$ cathode with carbon coated Al and bare Al current collector, respectively. EIS of cathode material can be divided into three regions, (1) high frequency (resistance due to surface film), (2) midfrequency (charge transfer resistance), and (3) solid state diffusion (Warburg factor/resistance). From Figure 6a, it can be seen that carbon-coated Al current collector sample shows additional loop at high frequency (Figure 6a inset) and during discharge and charge process, Figure 6b), respectively. This small loop/semicircle is due to the interface between the carbon layer and the current collector. Thus, the semicircles for the carbon-coated Al current collector is attributed to resistance between the carbon film and current collector interface; resistance through the solid electrolyte interface (SEI) film formed on the cathode surface and charge transfer resistance due to the cathode film and electrolyte solution interface. The fitted models are shown in Figure 7. EIS during the discharge process for OCV (~3.0 V), 2.5, and 1.9 V is fitted with circuit 1 (Figure 7), and for 1 V the data is fitted with circuit 2. It is well illustrated from the EIS experiment for 1 V, at lower frequency regions, the curve deviated from 45° toward higher angle suggests the interfacial storage, thus element M_2 (fitting parameter available with Biologic software) is added in place of pure diffusion. Similarly, during the charge process for the carbon-coated Al current collector (Figure 6b), the loop in the high-frequency region was observed (data fitted with circuit 1). However, for bare Al-current collector the EIS (Figure 6c,d) is fitted with two parallel RC circuits (circuit 3) with Warburg resistance at lower frequency. More interestingly, the effect of modification of current collector is visible with the fitted data of EIS. The charge transfer resistance (R_{ct}) for $NH_4V_4O_{10}$ cathode with both current collectors is shown in Figure S7a,b. With insertion of Na^+, R_{ct} of the $NH_4V_4O_{10}$ cathode increases for both current collectors. The analysis shows a clear difference between current collectors, where at OCV for carbon-coated and bare Al current collectors, the R_{ct} was ~57 and ~84 Ω, respectively. Moreover, at 1.9 and 2.5 V (discharge process, carbon-coated Al current collector), which is the biphasic zone for the $NH_4V_4O_{10}$ cathode, R_{ct} remains constant; whereas, during charge process at 2.0 and 2.5 V, variation was negligible. We can conclude from this section that R_{ct} for the $NH_4V_4O_{10}$ cathode with carbon-coated Al current collector was minimum compared with bare Al current collector. Thus, improved/enhanced performance was achieved for $NH_4V_4O_{10}$ cathode with carbon coated Al-current collector.

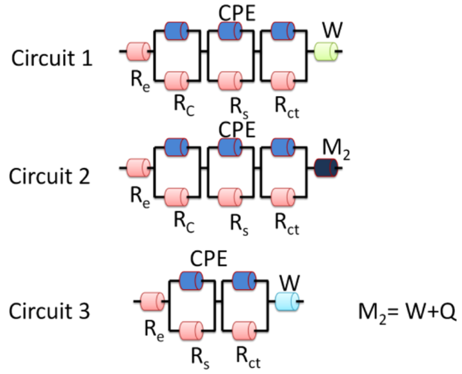

Figure 7. Equivalent circuit for EIS.

Further, Figure 8 shows the comparative results of literature and present result of vanadium-based cathode material for NIB. Su et al. synthesized bilayered V_2O_5 nanobelts which delivered initial discharge capacity of ~195 mAh g^{-1} at the current rate of 160 mA g^{-1} with 81% capacity retention after 50 cycles.[9] Further, Tepavcevic et al. demonstrate V_2O_5 as NIB cathode material with initial discharge capacity of 250 mAh g^{-1} at very low current density of 20 mA g^{-1}.[10] Similarly, $(NH_4)_2V_6O_{16}$ was used as cathode for NIB and delivered an initial discharge capacity of 180 mAh g^{-1} at an intermediate current density of 100 mA g^{-1} with poor cyclic stability (65% retention of discharge capacity after 50 cycle).[15] Fei et al. reported $NH_4V_4O_{10}$ cathode material which delivered initial discharge capacity of 121 mAh g^{-1} at the current density of 200 mA g^{-1}; however, stable cyclic performance was achieved after initial capacity loss with addition of 5% FEC as an additive in the electrolyte.[16] Whereas, $NH_4V_4O_{10}$ cathode retained its initial discharge capacity of ~82% after 50 cycle.[16] Raju et al. demonstrate the vanadium oxide as NIB cathode material which deliverer low initial discharge capacity ~120 mAh g^{-1} at current density of 160 mA g^{-1} with 54% retention of initial discharge after 50 cycles.[25] Whereas, the material in the present study not only demonstrates high rate performance but also delivers better cyclic stability. $NH_4V_4O_{10}$ nanobelts delivered initial discharge capacity ~191 mAh g^{-1} at high current rate of 200 mA g^{-1} with capacity retention of 88% after 50 cycles without any addition of additive to the electrolyte. In this report, $NH_4V_4O_{10}$ nanobelts as NIB cathode material with excellent electrochemical performances were demonstrated. Improvement of performances was achieved with carbon-coated Al current collector in a potential cutoff range of 1.5−3.5 V.

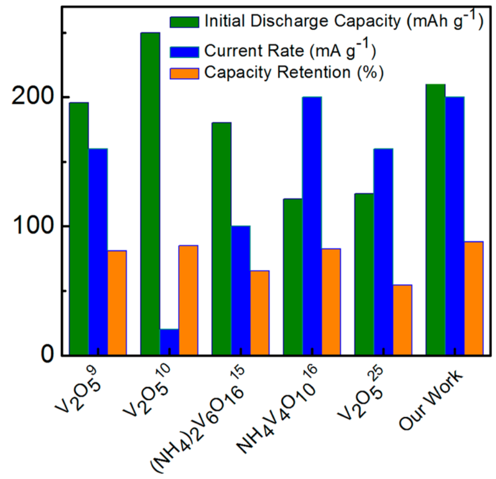

Figure 8. Comparative results of vanadium-based cathode for NIB.

CONCLUSION

In brief, we have synthesized nanodimension $NH_4V_4O_{10}$ material as suitable candidate for Na^+ storage with promising electrochemical performance. Nanostructured $NH_4V_4O_{10}$ materials were synthesized via a single step hydrothermal process. Further, elongation of $NH_4V_4O_{10}$ nanobelts toward the *c* axis and minimum growth toward the *b* axis, that is, [0*k*0] results in a faster Na^+ transport. It was further noticed that the insertion of Na^+ into the host matrix in a potential window of 1−4 V leads to a capacity fading due to untoward reactions; however, improved capacity was achieved in a potential window of 1.5−3.5 V. Though, capacity improvement was observed with potential cutoff, further improvement in electrochemical performances was achieved with the use of carbon-coated Al current collector. A detailed ab initio study was performed, and the results are well correlated with the experimental results. We believe further optimization of morphology and electrode design will help us to achieve even higher capacity and longer cyclic life cathode materials for NIB. The study of the compatibility of $NH_4V_4O_{10}$ cathode with some alloy-based anode materials such as Sn and SnO_2 also deserves further investigation to harvest the full capacity of the present cathode material.

■ ASSOCIATED CONTENT

Ⓢ Supporting Information

Details of theoretical calculation; configuration of the $Na_3NH_4V_4O_{10}$, $Na_1NH_4V_4O_{10}$, $Na_{0.5}NH_4V_4O_{10}$, and $NH_4V_4O_{10}$; calculated formation energies of $NH_4V_4O_{10}$ structure with Na in gallery space and within the layer; FEG-SEM image of $NH_4V_4O_{10}$ nanobelts; FEG-TEM image and HR-TEM image of $NH_4V_4O_{10}$ material (after 25th cycle). FEG-TEM image of $NH_4V_4O_{10}$ material (after 32nd cycle); first charge/discharge profile of $NH_4V_4O_{10}$ cathode material between varying potential (bare Al current collector), discharge capacity vs cycle number (bare Al current collector), first charge/discharge of $NH_4V_4O_{10}$ cathode material between 1.5 and 3.5 V at varying current rate with carbon coated Al-current collector, discharge capacity vs cycle number between 1.5 and 3.5 V at varying current rates with carbon-coated Al current collector; R_{ct} of carbon-coated and bare Al current collector during discharge process, charge process; discharge capacity of carbon at 200 mA g^{-1} current rate in potential window 1.5–3.5 V; magnetic moment of all the vanadium atoms in $Na_xNH_4V_4O_{10}$ from DFT calculations; and calculated lattice parameters and lattice volume at different concentration of Na in $NH_4V_4O_{10}$. The Supporting Information is available free of charge on the ACS Publications website at DOI: 10.1021/acsami.5b03210.

■ AUTHOR INFORMATION

Corresponding Author

* Tel: + 91-222576-7849. E-mail: sagar.mitra@iitb.ac.in.

Author Contributions

The manuscript was written through contributions of all authors. All authors have given approval to the final version of the manuscript.

Funding

The reported work is equally supported by U.S.–India Partnership to Advance Clean Energy-Research (PACE-R) for the Solar Energy Research Institute for India and the United States (SERIIUS) and National Centre for Photovoltaic Research and Education (NCPRE)-Ministry of New and Renewable Energy. SERIIUS project is funded jointly by the U.S. Department of Energy (Office of Science, Office of Basic Energy Sciences, and Energy Efficiency and Renewable Energy, Solar Energy Technology Program, under Subcontract DE-AC36-08GO28308 to the National Renewable Energy Laboratory, Golden, Colorado) and the Government of India through the Department of Science and Technology under Subcontract IUSSTF/JCERDC-SERIIUS/2012 dated 22 Nov. 2012.

Notes

The authors declare no competing financial interest.

■ ACKNOWLEDGMENTS

The authors are indebted to SAIF, IIT-B for their assistance in FEG-TEM, to NCPRE for FEG-SEM facility, and to DESE for XRD analysis. We are thankful to MNCF, IISc, Bangalore, for their assistance in XPS study.

■ REFERENCES

(1) Slater, M. D.; Kim, D.; Lee, E.; Johnson, C. S. Sodium-Ion Batteries. *Adv. Funct. Mater.* **2013**, *23*, 947–958.

(2) Hong, J.; Wang, X.-L.; Wang, Q.; Omenya, F.; Chernova, N. A.; Whittingham, M. S.; Graetz, J. Structure and Electrochemistry of Vanadium-Modified $LiFePO_4$. *J. Phys. Chem. C* **2012**, *116*, 20787–20793.

(3) Harrison, K. L.; Bridges, C. A.; Paranthaman, M. P.; Segre, C. U.; Katsoudas, J.; Maroni, V. A.; Idrobo, J. C.; Goodenough, J. B.; Manthiram, A. Temperature Dependence of Aliovalent-Vanadium Doping in $LiFePO_4$ Cathodes. *Chem. Mater.* **2013**, *25*, 768–781.

(4) Janssen, Y.; Middlemiss, D. S.; Bo, S. H.; Grey, C. P.; Khalifah, P. G. Structural Modulation in the High Capacity Battery Cathode Material $LiFeBO_3$. *J. Am. Chem. Soc.* **2012**, *134*, 12516–12527.

(5) Singh, S.; Mitra, S. Improved Electrochemical Activity of Nanostructured Li_2FeSiO_4/MWCNTs Composite Cathode. *Electrochim. Acta* **2014**, *123*, 378–386.

(6) Tamaru, M.; Chung, S. C.; Shimizu, D.; Nishimura, S.-I.; Yamada, A. Pyrophosphate Chemistry Toward Safe Rechargeable Batteries. *Chem. Mater.* **2013**, *25*, 2538–2543.

(7) Sarkar, S.; Mitra, S. $Li_3V_2(PO_4)_3$ Addition to the Olivine Phase: Understanding the Effect in Electrochemical Performance. *J. Phys. Chem. C* **2014**, *118*, 11512–11525.

(8) Barpanda, P.; Oyama, G.; Nishimura, S.-I.; Chung, S.-C.; Yamada, A. A 3.8-V Earth-Abundant Sodium Battery Electrode. *Nat. Commun.* **2014**, *5*, 4358.

(9) Su, D.; Wang, G. Single-Crystalline Bilayered V_2O_5 Nanobelts for High-Capacity Sodium-Ion Batteries. *ACS Nano* **2013**, *7*, 11218–11226.

(10) Tepavcevic, S.; Xiong, H.; Stamenkovic, V. R.; Zuo, X.; Balasubramanian, M.; Prakapenka, V. B.; Johnson, C. S.; Rajh, T. Nanostructured Bilayered Vanadium Oxide Electrodes for Rechargeable Sodium-Ion Batteries. *ACS Nano* **2012**, *6*, 530–538.

(11) Hartung, S.; Bucher, N.; Nair, V. S.; Ling, C. Y.; Wang, Y.; Hoster, H. E.; Srinivasan, M. Sodium Vanadium Oxide: A New Material for High Performance Symmetric Sodium-Ion Batteries. *ChemPhysChem* **2014**, *15*, 2121–2128.

(12) Sarkar, S.; Banda, H.; Mitra, S. High Capacity Lithium-Ion Battery Cathode Using LiV_3O_8 Nanorods. *Electrochim. Acta* **2013**, *99*, 242–252.

(13) Sarkar, S.; Bhowmik, A.; Bharadwaj, M. D.; Mitra, S. Phase Transition, Electrochemistry, and Structural Studies of High Rate $Li_xV_3O_8$ Cathode with Nanoplate Morphology. *J. Electrochem. Soc.* **2014**, *161*, A14–A22.

(14) Sarkar, S.; Veluri, P. S.; Mitra, S. Morphology Controlled Synthesis of Layered $NH_4V_4O_{10}$ and the Impact of Binder on Stable High Rate Electrochemical Performance. *Electrochim. Acta* **2014**, *132*, 448–456.

(15) Fei, H.; Liu, X.; Li, H.; Wei, M. Enhanced Electrochemical Performance of Ammonium Vanadium Bronze Through Sodium Intercalation and Optimization of Electrolyte. *J. Colloid Interface Sci.* **2014**, *418*, 273–276.

(16) Fei, H.; Liu, X.; Lin, Y.; Wei, M. Facile Synthesis of Ammonium Vanadium Oxide Nanorods for Na-Ion Battery Cathodes. *J. Colloid Interface Sci.* **2014**, *428*, 73–77.

(17) Yabuuchi, N.; Kubota, K.; Dahbi, M.; Komaba, S. Research Development on Sodium-Ion Batteries. *Chem. Rev.* **2014**, *114*, 11636–11682.

(18) Lee, K. T.; Cho, J. Role of Nanosize in Lithium Reactive Nanomaterial for Lithium Ion Batteries. *Nano Today* **2011**, *6*, 28–41.

(19) West, K.; Zachau-Christiansen, B.; Jacobsen, T.; Atlung, S. V_6O_{13} as Cathode Material for Lithium Cells. *J. Power Sources* **1985**, *14*, 235−245.

(20) Rodríguez-Carvajal, J. Recent Advances in Magnetic Structure Determination Neutron Powder Diffraction. *Phys. B* **1993**, *192*, 55−69.

(21) Van Der Ven, A.; Bhattacharya, J.; Belak, A. A. Understanding Li Diffusion in Li Intercalation Compounds. *Acc. Chem. Res.* **2013**, *46*, 1216−1225.

(22) Li, D.; Zhou, H. Two-phase transition of Li-intercalation compounds in Li-ion batteries. *Mater. Today* **2014**, *17*, 451−463.

(23) Prado-Gonjal, J.; Molero-Sánchez, B.; Ávila-Brande, D.; Morán, E.; Pérez-Flores, J. C.; Kuhn, A.; García-Alvarado, F. The Intercalation Chemistry of $H_2V_3O_8$ NanobeltsSynthesised by a Green, Fast and Cost-Effective Procedure. *J. Power Sources* **2013**, *232*, 173−180.

(24) Chernova, N. A.; Roppolo, M.; Dillon, A. C.; Whittingham, M. S. Layered Vanadium and Molybdenum Oxides: Batteries and Electrochromics. *J. Mater. Chem.* **2009**, *19*, 2526−2252.

(25) Raju, V.; Rains, J.; Gates, C.; Luo, W.; Wang, X.; Stickle, W. F.; Stucky, G. D.; Ji, X. Superior Cathode of Sodium-Ion Batteries: Orthorhombic V_2O_5 Nanoparticles Generated in Nanoporous Carbon by Ambient Hydrolysis Deposition. *Nano Lett.* **2014**, *14*, 4119−4124.